

Preferential concentration of poly-dispersed droplets in stationary isotropic turbulence

Huan Lian · Georgios Charalampous ·
Yannis Hardalupas

Received: 11 November 2012 / Revised: 14 April 2013 / Accepted: 17 April 2013 / Published online: 9 May 2013
© Springer-Verlag Berlin Heidelberg 2013

Abstract The preferential concentration of poly-dispersed water droplets with a range of Sauter mean diameters between 25 and 95 μm has been studied experimentally in stationary homogeneous isotropic turbulence with four different intensities, characterized by turbulent Reynolds numbers based on Taylor microscale, of $Re_\lambda = 107, 145, 185$ and 213. The image processing method of recorded scattered light intensity images from droplets is described and its ability to identify droplets is assessed in terms of image quality. The influence of image processing parameters on measured characteristics of droplet clustering is evaluated. The radial distribution function (RDF) and 2D Voronoï analysis quantified the magnitude of preferential droplet concentration and the results from both methods agreed well. RDF showed that the characteristic length scale of resulting droplet clusters varies between 20 and 30 times the Kolmogorov length scale over all the experimental conditions. It was found that the preferential concentration is more appropriately described by a Stokes number, based on various representative diameters, namely the arithmetic mean diameter, D_{10} , or the diameter, $DN_{60\%}$, below which 60 % of the total droplet number in the spray is present, or the diameter, $DV_5\%$, which carries 5 % of the total liquid volume in the spray. The magnitude of droplet preferential concentration

was maximum when the proposed Stokes number was around unity for all experimental conditions. Little dependence of the magnitude of preferential concentration on turbulent Reynolds numbers was found, in contrast to the recent DNS findings (Tagawa et al. in J Fluid Mech 693:201–215, 2012).

1 Introduction

It has been found (e.g. Crowe et al. 1985; Maxey 1987; Hardalupas et al. 1990, 1992; Squires and Eaton 1991; Longmire and Eaton 1992; Eaton and Fessler 1994) that when droplet response time is similar to a turbulent characteristic time, droplets tend to preferentially concentrate within regions of low vorticity and high strain rate and form clusters. The formation of clusters has profound influence on particle settling (Wang and Maxey 1993; Aliseda et al. 2002), spray combustor performance (Zimmer et al. 2003) and development of convective clouds in warm rain initiation (Sundram and Collins 1997; Shaw et al. 1998; Siebert et al. 2010).

The quantification of preferential concentration has been widely studied numerically during the past two decades based on direct numerical simulation (DNS), as reviewed recently by Salazar and Collins (2009) and Balachandar and Eaton (2010). However, experimental studies remain scarce (Wood et al. 2005; Salazar et al. 2008; Saw et al. 2008; Monchaux et al. 2010; Bateson and Aliseda 2012). Wood et al. (2005) applied the ‘box counting’ method (Fessler et al. 1994) and the two-dimensional radial distribution function (RDF) (Sundram and Collins 1999) to quantify mono-dispersed solid particle preferential concentration within homogeneous and isotropic turbulence with very small mean flow. Strongest clustering was found

Originally presented in 16th Int Symp on Applications of Laser Techniques to Fluid Mechanics Lisbon, Portugal, 09–12 July, 2012.

This article is part of the Topical Collection on Application of Laser Techniques to Fluid Mechanics 2012.

H. Lian · G. Charalampous · Y. Hardalupas (✉)
Department of Mechanical Engineering, Imperial College
London, London SW7 2AZ, UK
e-mail: y.hardalupas@imperial.ac.uk

to occur at a length scale of 10 times the Kolmogorov length scale for particle Stokes number near unity. Salazar et al. (2008) presented three-dimensional RDF quantification of solid particle preferential concentration within homogeneous and isotropic turbulence with small mean flow by acquiring information with holographic particle image velocimetry (PIV) and compared the experimental results with DNS simulations. Saw et al. (2008) performed particle pair correlation to study clustering of high mass loading inertial water droplets generated by four spray nozzles in a wind tunnel with high turbulent Reynolds number. Monchaux et al. (2010) proposed a Voronoï analysis to quantify preferential concentration of poly-dispersed droplets generated by air-assist atomizer in isotropic turbulence with conveying mean flow in a wind tunnel. Bateson and Aliseda (2012) studied experimentally the influence of preferential concentration, evaluated by RDF method, on droplets collisions and concluded that both preferential concentration and enhanced settling can lead to significant increase in collision probability of inertial droplets with size between 10 and 50 μm .

In previous studies, the preferential concentration was studied with both mono-dispersed solid particles (Wood et al. 2005) and poly-dispersed droplets (Saw et al. 2008; Monchaux et al. 2010; Bordás et al. 2011; Bateson and Aliseda 2012). Studies with poly-dispersed droplets used various definitions of mean diameters to characterize the droplets and their dispersion. However, in the presence of wide size spread of polydispersed droplet size distributions, various approaches to define droplet mean size result in large variation of values of the Stokes number, for which maximum droplet clustering occurs. In addition, descriptions and evaluation of image processing methods for particle identification for the quantification of clustering behaviour are limited in the literature (Fallon and Rogers 2002; Salazar et al. 2008). Thus, the objectives of the present paper are to:

(1) propose an image processing procedure for droplet identification and provide assessment of its performance in quantifying clustering behaviour; (2) propose a scaling method for clustering behaviour of poly-dispersed droplets, based on a Stokes number related to an ‘appropriate’ representative droplet; and (3) quantify the length scale of droplet clusters and its dependence on droplet size distribution and flow turbulent Reynolds number.

The next section describes the experimental arrangement, the droplet characteristics and the image processing approach. Section 3 quantifies droplet clustering characteristics, based on RDF approach and Voronoï analysis, and proposes a scaling approach based on an ‘appropriate’ droplet Stokes number. Section 4 presents the dependence of droplet clustering on flow turbulent intensity and the paper ends with a summary of the main findings.

2 Experimental set-up

Homogeneous and isotropic turbulence with four different intensities represented by turbulent Reynolds number $Re_\lambda = 107, 145, 185, 213$, based on the Taylor microscale, and zero mean velocity has been generated within a volume of 40 mm³ in the facility referred to as ‘box of turbulence’ described below. Droplets with different size spread of the size distribution and Sauter mean diameters ranging from 25 to 95 μm have been generated and introduced into the ‘box of turbulence’ continuously with an air-assist atomizer. Due to the low droplet volume fraction of around 8×10^{-6} , we assume one-way coupling between the two phases, no air flow turbulence modification by droplets and negligible probability of inter-droplet collisions.

2.1 Turbulence generation and characterization

The stationary homogeneous and isotropic turbulence has been generated in a facility, generally referred to as ‘box of turbulence’, implemented by Charalampous and Hardalupas (2010), following the idea of Birouk et al. (1996), Hwang and Eaton (2004) and Goepfert et al. (2009). The ‘box of turbulence’ was built as a cubic frame constructed with 1-m length aluminium profiles. Eight loudspeakers from Davis acoustic (Model No. 20MC8A) were mounted on specially designed aluminium plates installed at eight corners of the cubic box, all pointing at the centre of the cubic box. The vibrations of the membranes of the speakers induced ambient air motions and delivered arrays of 55 jets produced by perforated PVC plates with 6-mm-diameter holes arranged in a triangular pattern and placed in front of each loudspeaker. Four pairs of opposing jet arrays were set up with a distance of 590 mm between each opposing pair. Each loudspeaker was driven by a sine wave with random frequencies ranging from 40 to 60 Hz. The eight sine waves were generated by a 16 bit National Instruments analogue output card with 8 channels (PCI6733) and amplified by Behringer Europower EP2500 audio stereo amplifiers. The experimental arrangement of the ‘box of turbulence’ with eight loudspeakers can be seen in Fig. 1a, b.

The instantaneous velocity of the air flow turbulence was measured by PIV. The laser beam was generated by a New Wave Nd:YAG laser at 532 nm with maximum energy of 120 mJ per pulse. Glycol droplets with size less than 3 microns were introduced in the flow for the PIV measurements of the gas flow. The measurement area was illuminated twice with a small time difference by a laser sheet, which was generated from the laser beam by a series of cylindrical lenses. The waist of the laser sheet was about 0.5 mm, with the focal length of 0.4 m. The displacements of tracer particles were recorded as double-frame/double exposure with a PCO Sensicam inter-frame CCD camera

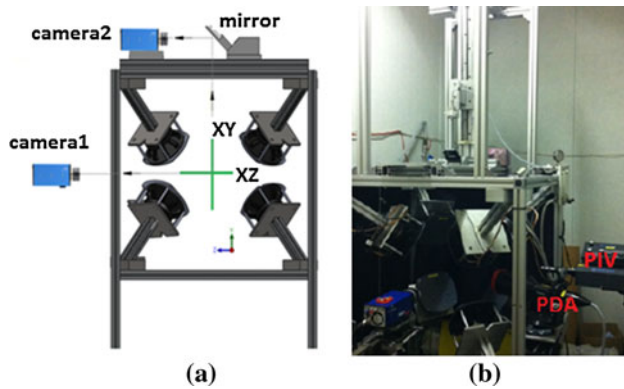


Fig. 1 **a** Schematic of two cameras set-up for 3D PIV velocity measurement and coordinate system of 'box of turbulence' facility; **b** photograph of the experimental set-up of the 'box of turbulence', which shows the PIV and Phase Doppler Anemometry (PDA) instruments and the water injection arrangement at the top of the flow

with a resolution of $1,376 \times 1,040$ pixels with spatial resolution of $58 \mu\text{m}/\text{pixel}$. Two identical recording cameras are arranged to achieve PIV measurements on two normal planes, as shown in Fig. 1a. The first camera records particle images on the XY plane, while the second camera records particle images in the XZ plane. By introducing a mirror placed 45° to the plane XZ, both cameras can be installed in parallel with the first camera placed perpendicular to the laser sheet and the second camera placed parallel to the laser sheet. This arrangement of the cameras makes the optical alignment easier. Illumination of the two crossing XY and XZ planes can be achieved by rotating the laser sheet optics by 90° . Combining the recorded information from the two cameras, the carrier phase velocity is measured in all three directions. The two-camera arrangement enabled a more efficient approach to evaluate the characteristics of the flow turbulence and establish that it was stationary and isotropic along both planes. After establishing that the turbulence was stationary by considering the mean velocity vector on both XY and XZ planes, the instantaneous velocity vectors on plane XY were used to evaluate the isotropy of the turbulence. All the measurements of droplet characteristics were obtained on XY plane.

The characterization of the stationary homogeneous and isotropic turbulence is briefly presented below for flow with $Re_\lambda = 185$. The spatial mean flow velocity is less than 0.1 m/s everywhere (Fig. 2a) and demonstrates that the local flow is stationary. The contours of the ratio of the rms of velocity fluctuations $u_{1,\text{rms}}/u_{2,\text{rms}}$ are presented in Fig. 2b to demonstrate the homogeneity of the flow. Note that $u_{1,\text{rms}}$ is 0.53 m/s and $u_{2,\text{rms}}$ is 0.54 m/s for $Re_\lambda = 185$. A central area of $40 \text{ mm} \times 40 \text{ mm}$ is the area of interest. The isotropy of the turbulent flow generated at the central area of the 'box of turbulence' is demonstrated by the spatial

correlation coefficient of the velocity fluctuations between two neighbouring points, as calculated from the instantaneous flow field velocity information. The two-point longitudinal velocity correlation coefficients in x and y directions are defined as a function of the distance r between the two points as:

$$F_{11}(r) = \frac{\langle u_1(x_1, x_2) u_1(x_1 + r, x_2) \rangle}{\overline{u_{1,\text{rms}}^2}} \quad (1)$$

$$F_{22}(r) = \frac{\langle u_2(x_1, x_2) u_2(x_1, x_2 + r) \rangle}{\overline{u_{2,\text{rms}}^2}} \quad (2)$$

The lateral velocity correlation coefficient in x and y directions is defined as

$$G_{11}(r) = \frac{\langle u_1(x_1, x_2) u_1(x_1, x_2 + r) \rangle}{\overline{u_{1,\text{rms}}^2}} \quad (3)$$

$$G_{22}(r) = \frac{\langle u_2(x_1, x_2) u_2(x_1 + r, x_2) \rangle}{\overline{u_{2,\text{rms}}^2}} \quad (4)$$

A relationship between the longitudinal and lateral velocity correlation coefficients in isotropic turbulence was proposed by Batchelor (1953):

$$G(r) = F(r) + \frac{r}{2} \frac{\partial F(r)}{\partial r} \quad (5)$$

No parabolic behaviour can be observed at the origin due to lack of spatial resolution. The values of the correlations did not reach to zero because the measurement domain was too small. Therefore, we estimated the integral length scale by integrating the correlation function after extrapolating it at large radial distances using a polynomial function, following Teutolsky et al. (1992). The integration process followed the approach of George (2006). However, it should be noted that the estimated integral length scale has some uncertainty due to the extrapolation process. For the presented flow with $Re_\lambda = 185$, the estimated integral length scale was calculated from u vector and v vector to be about 42.2 and 43.5 mm , respectively. A good agreement between the x and y directions of both the longitudinal and the lateral spatial velocity correlation coefficient calculated from the measured instantaneous velocity fields (Fig. 2b, c) as well as the estimated integral length scale supports the isotropy of turbulence. The experimental results also agree with the theoretical expectation of Eq. (5), as shown in Fig. 2c, which is reached for a radius more than 40 mm , and confirms that isotropy was achieved in the area of interest. Therefore, the turbulent flow is confirmed as homogeneous and isotropic.

The turbulent energy dissipation rate $\varepsilon (\text{m}^2/\text{s}^3)$ is obtained with the direct method described by Jong et al. (2008) under the assumptions of homogeneity and isotropy. Other turbulent scaling quantities were calculated based on the dissipation rate with the following definitions. Turbulence quantities for each of the four flow conditions are presented in Table 1.

Fig. 2 **a** Contours of mean velocity on the XY plane; **b** contours of the ratio of velocity fluctuations $u_{1,rms}/u_{2,rms}$; **c** two-point velocity correlation coefficients. The flow in the ‘Box of Turbulence’ is for turbulent Reynolds number $Re_\lambda = 185$

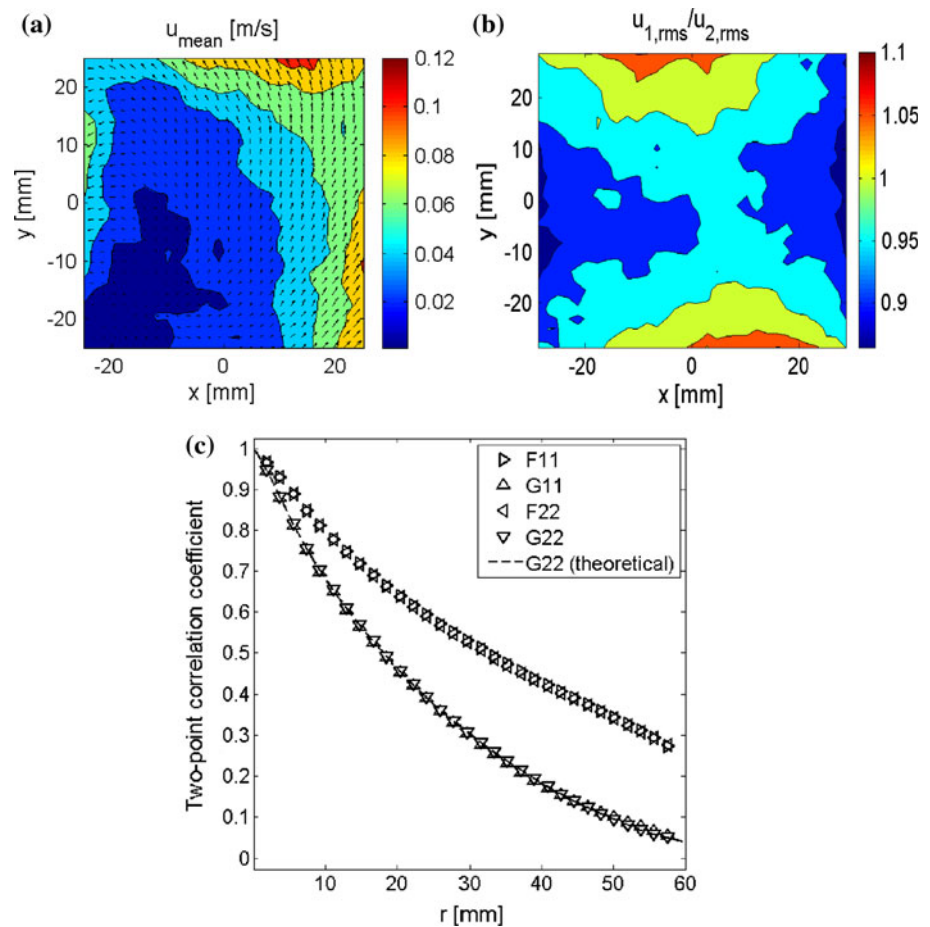


Table 1 Summary of the experimental flow conditions in the ‘box of turbulence’

Flow	Re_λ	τ_k (m s)	ε (m ² /s ³)	q^2 (m ² /s ²)	η (mm)	τ_e (s)	\bar{u}_1, rms (m/s)	\bar{u}_2, rms (m/s)
1	107	3.4	1.28	0.36	0.23	0.14	0.35	0.35
2	145	3.2	1.48	0.52	0.22	0.18	0.42	0.42
3	185	2.5	2.38	0.85	0.19	0.18	0.53	0.54
4	213	2.2	3.15	1.13	0.18	0.18	0.61	0.62

The turbulent kinetic energy is defined as

$$q^2(x, y) \cong 3 \frac{u_{1,rms}^2(x, y) + u_{2,rms}^2(x, y)}{2} \quad (6)$$

The Reynolds number associated with Taylor microscale is

$$Re_\lambda \cong \frac{\lambda(q^2/3)^{1/2}}{\nu} \quad (7)$$

where ν is the kinematic viscosity of the air, which is 1.57×10^{-5} m²/s at atmospheric pressure and temperature, and λ is the Taylor length scale defined as

$$\lambda \cong \left(\frac{5\nu q^2}{\varepsilon} \right)^{1/2} \quad (8)$$

and valued 5.29 mm for the flow with $Re_\lambda = 185$. The Taylor microscale was estimated from the turbulent dissipation rate. It was not calculated from the curvature of the correlation function because the parabolic behaviour could not be observed at the origin of the correlations due to the limited spatial resolution. The corresponding Eulerian timescale (eddy turnover time) was defined as

$$\tau_e \cong \left(\frac{q^2/2}{\varepsilon} \right) \quad (9)$$

The Kolmogorov time and length scale τ_k and η , respectively, are defined as below and valued 2.5 ms and 0.19 mm for the condition $Re_\lambda = 185$.

$$\tau_k \cong \left(\frac{\nu}{\varepsilon} \right)^{1/2} \quad (10)$$

$$\eta \cong \left(\frac{v^3}{\varepsilon} \right)^{1/4} \quad (11)$$

It should be noted that the instantaneous droplet images were acquired by using a laser repetition rate of 5 Hz, which led to a sampling interval time of 0.2 s. This is longer than the corresponding eddy turn of 0.18 s (Table 1), and in this way, the acquired instantaneous images remained statistically independent.

2.2 Droplet injection and characterization

Poly-dispersed droplets are generated by an air-assist atomizer. The droplet sizes are controlled by adjusting the inlet water flow rate and air pressure. Larger droplet mean diameters can be achieved by increasing the water flow rate, while keeping the air pressure constant. The atomizer was installed at the top of the ‘box of turbulence’ with an adjustable positioning device, in order to optimize the operation for various experimental conditions. The atomizer nozzle was placed 0.8 m above the central region of the ‘box of turbulence’. This ensured that the droplet momentum was negligible when entering the ‘box’. The droplet size distributions present in the ‘box’ of turbulence were measured by a fibre Phase Doppler Anemometry (PDA) system (57X80) from Dantec forming an optical focusing probe volume at the centre of the ‘box of turbulence’ (Fig. 1b). The optical set-up of the PDA allowed a maximum droplet size of 160 μm to be measured.

To acquire sufficient data to describe the droplet size distribution, 1,500–9,000 validated droplets were measured for each experiment. Sample measurements of droplet size distributions generated by the air-assist atomizer are shown in Fig. 3a. The typical statistical uncertainty for the measured droplet size distributions and representative mean diameters was around 3 % based on the number of samples that were considered, following suggestions of Tate (1982). The main statistical parameters applied to quantify the droplet size are the droplet arithmetic mean diameter, D_{10} , and the Sauter mean diameter—the ratio of the droplet volume to droplet surface area D_{32} . These were calculated according to the general definition of Eq. (12) (Bayvel and Orzechowski 1993):

$$Dpq = \sqrt[p-q]{\frac{\sum_{i=1}^m D_i^p \Delta n_i}{\sum_{i=1}^m D_i^q \Delta n_i}} \quad (12)$$

Number-weighted droplet size distributions for different operating conditions of the atomizer, measured within the flow with turbulent Reynolds number of 185, are shown in Fig. 3a. The corresponding droplet cumulative size distributions are shown in Fig. 3b. The droplet number-based diameters $DN_{x\%}$ representing diameters

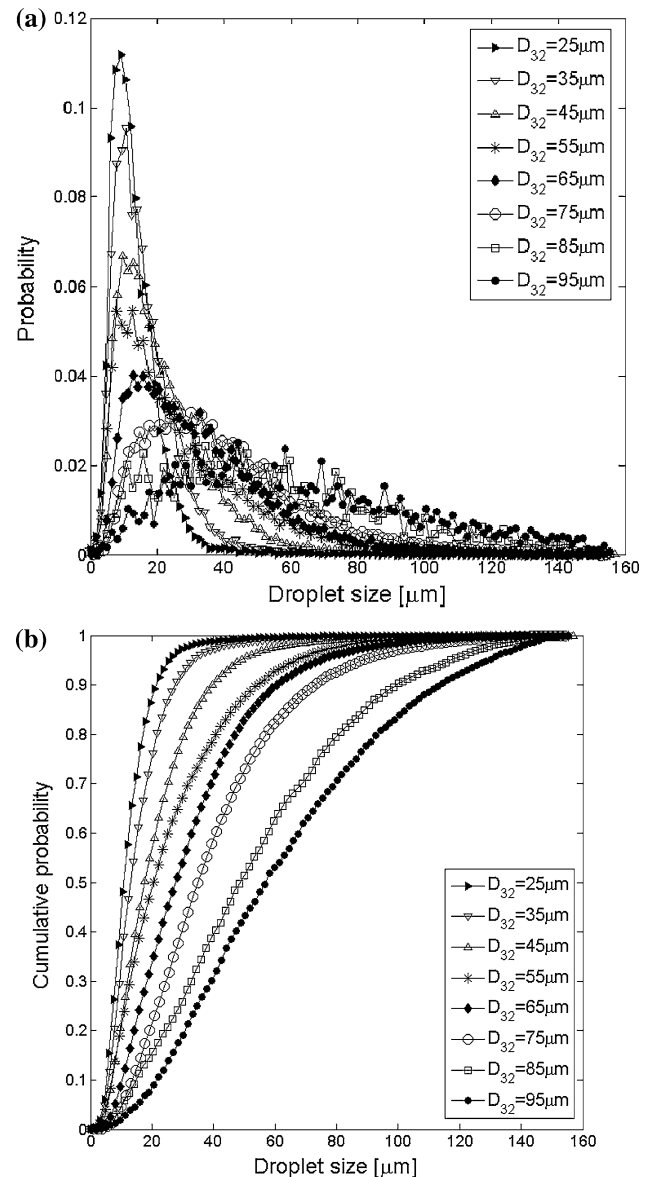


Fig. 3 **a** Number-weighted droplet size distributions; **b** cumulative number-weighted distributions as a function of droplet size. Flow with turbulent Reynolds number Re_λ of 185

carrying different fractions of the cumulative number of droplets in a size distribution and droplet volume-based diameters $DV_{x\%}$ representing diameters carrying different fractions of the cumulative volume of the droplet size distribution were calculated. The reader is also referred to Fig. 13 for the relevant definitions of the representative diameters for a specific size distribution. $DN_{40\%}$ and $DN_{60\%}$ are derived from the cumulative droplet number-based size distributions and indicate respectively the diameters below which 40 and 60 % of the total number of droplets in the spray are present. Representative droplet diameters based on a number-weighted size distribution may be more appropriate for scaling the

behaviour of preferential concentration, which is identified by droplet clusters with large number density and voids with low number density of droplets relative to the average across the imaging region. Volume-weighted size distributions and the corresponding cumulative distributions are also commonly used and are converted from number-weighted distributions after considering the volume of each droplet size. Representative diameters, $DV_x\%$, associated with volume-based size distributions, are those below which the respective fraction x of the total liquid volume in the spray is present. The droplet size spread is also characterized based on the volume-based size distribution with relative diameter span factor (Δ_{RSF}) defined in Eq. (13) (Bayvel and Orzechowski 1993; Lefebvre 1989).

$$\Delta_{RSF} = \frac{DV_{90\%} - DV_{10\%}}{DV_{50\%}} \quad (13)$$

Although the droplet size measurements were obtained at the centre of the ‘box of turbulence’, the droplet size distributions remained the same within the statistical

uncertainty of the measurements elsewhere. This was verified by obtaining measurements at different locations, which are not presented here. This is expected due to the lack of droplet momentum when entering the ‘box’. Each measurement represents one set of experiments and is characterized by the droplet Sauter mean diameter D_{32} [Eq. (12)] ranging from 25 to 95 μm . Different size spreads have been achieved and characterized accordingly for each experiment.

Experiments on quantification of droplet clustering were limited to droplet size distributions with relatively narrow size spreads, and for this reason, the range of the considered Sauter mean diameters was limited between 25 and 75 μm . However, the proposed image processing method has been applied and tested for experiments with droplet Sauter mean diameter in the full range of 25–95 μm . A summary of the various representative droplet diameters and droplet size spread of the size distributions for four different turbulent Reynolds numbers is shown in Table 2. The considered diameters are D_{10} and D_{32} according to the definition of Eq. (12); for example, $DN_{40\%}$ of 4.3 microns

Table 2 Characteristics of droplet present in the turbulent flow with $Re_\lambda = 107, 145, 185$ and 213

Droplet info exp. no.	D_{10} (μm)	D_{32} (μm)	$DN_{40\%}$ (μm)	$DN_{60\%}$ (μm)	$DV_5\%$ (μm)	$DV_{50\%}$ (μm)	Δ_{RSF}
$Re_\lambda = 107$							
No. 1	8.5	$25_{+1.2}$	4.3	6.9	10.6	30.6	2.4
No. 2	11.2	$35_{+2.8}$	5.2	8.9	15.0	45.8	2.1
No. 3	14.1	$45_{+0.9}$	6.5	11.3	19.3	56.9	1.6
No. 4	16.5	$55_{-1.4}$	7.5	13.3	22.9	66.7	1.4
No. 5	21.0	$65_{-1.4}$	9.4	17.0	29.1	77.3	1.2
No. 6	25.3	$75_{-2.7}$	11.8	21.0	33.5	84.9	1.0
$Re_\lambda = 145$							
No. 1	7.2	$25_{-1.6}$	3.5	5.7	8.9	27.7	2.9
No. 2	9.0	$35_{-2.9}$	4.2	7.0	12.0	38.2	2.4
No. 3	13.6	$45_{+0.5}$	6.1	10.8	19.0	57.1	1.5
No. 4	17.5	$55_{+3.2}$	7.6	13.8	24.7	72.8	1.4
No. 5	20.2	$65_{+1.1}$	8.8	15.7	29.4	82.3	1.1
No. 6	27.4	$75_{+1.0}$	12.7	22.7	36.3	92.4	1.0
$Re_\lambda = 185$							
No. 1	13.3	$25_{+2.1}$	9.4	12.5	11.1	32.4	2.8
No. 2	16.4	$35_{+2.5}$	11.1	15.3	14.7	47.9	2.0
No. 3	22.1	$45_{+1.5}$	14.5	21.1	20.6	54.5	1.7
No. 4	27.1	$55_{+2.9}$	16.3	25.3	27.3	67.5	1.3
No. 5	33.2	$65_{-2.5}$	22.8	33.0	30.5	72.6	1.2
$Re_\lambda = 213$							
No. 1	13.5	$25_{+2.2}$	8.6	15.1	10.3	31.9	2.6
No. 2	17.5	$35_{+3.7}$	10.6	17.8	18.3	43.0	1.7
No. 3	21.9	$45_{+2.8}$	14	22.2	22.5	54.8	1.5
No. 4	25.6	$55_{-0.9}$	16.8	25.5	25.6	62.1	1.3
No. 5	32.0	$65_{-0.9}$	20.3	32.2	31.3	75.3	1.2

The subscripts in the D_{32} column show the measurement deviation from ideal case

means that 60 % of the droplets are larger than 4.3 microns, and $DV_{5\%}$ of 10.6 microns means that droplet with size larger than 10.6 microns represents 95 % of the total liquid volume. Finally, Δ_{RSF} characterizing the droplet size spread of the distribution is according to Eq. (13).

The gravitational settling velocity of the droplets was defined by Maxey (1987) as

$$W = \frac{m_p g}{6\pi r_p \mu} = \frac{\rho g d_p^2}{18\mu} \quad (14)$$

where μ is the dynamic viscosity of air at room temperature with the value of 1.9×10^{-5} kg/m/s; ρ is the density of water valued 1,000 kg/m³; g is the gravitational acceleration 9.8 m/s²; and d_p is the droplet diameter. A summary of droplet gravitational settling velocity and its ratio with turbulent velocity $u_{i,rms}$ is given in Table 3. The ratio of the droplet settling velocity and turbulent velocity fluctuations is less than 1 for all the experimental conditions, so that the influence of gravity is small compared to turbulent strain in the presented study.

2.3 Image acquisition and filtering

The scattered light from laser-illuminated water droplets has been recorded with single-frame-single-exposure images by a PCO Sensicam inter-frame CCD camera with a resolution of $1,024 \times 1,024$ pixels. The experimentally recorded images are stored as grey-scale TIFF formatted files. For each experimental flow condition with certain turbulent Reynolds number, 8 different droplet size distributions were injected, and for each condition, 1,000 instantaneous images were recorded. A total number of 32 experimental conditions have been studied for four different turbulent flow settings.

Fallon and Rogers (2002) applied image intensity threshold for image filtering and reported measurements, based on the assumption that intensity threshold does not affect measured statistics. This assumption may not be valid when poly-dispersed droplets are considered, since scattering intensity depends on droplet size. Salazar et al. (2008) used high-pass particle size threshold d_c for particle

identification and assumed a d_c level independent of experimental conditions. However, these studies did not evaluate the performance of the image processing methods on droplet identification and the measurement of droplet clustering characteristics. In this paper, we use an image processing method based on band-pass filtering (Crocker and Grier 1996) to generate binary images of identified droplets from the recorded grey-scale images. An evaluation of the processing method based on universal image quality Q index (Zhou and Bovik 2002) is presented, followed by the evaluation of the influence of different image processing parameters on quantifying preferential concentration. Each TIFF formatted image can be represented with a UINT8 image array, which assigns an integer between 0 and 255 to represent the intensity of each pixel, with the value 0 corresponding to black and 255 to white. The droplets are identified on the acquired instantaneous raw images using a band-pass filter. The cut-off values of the band-pass filtered image are established from the two-dimensional Gaussian convolution of the intensity as the high-pass filter and the boxcar convolution of the intensity as the low-pass filter. The processed final image is the difference between the Gaussian convoluted high-pass filtered image and the boxcar convoluted low-pass image. The image processing was developed within MATLAB environment. Binary images with identified droplets are achieved by calculating the local intensity maxima after the band-pass filter. These binary images are then further processed to quantify droplet preferential concentration.

The Gaussian convolution of the intensity determines the high-pass filter of the image processing in order to eliminate noise and smooth out the image with the 2D spatial isotropic kernel defined as:

$$G(x, y) = \frac{1}{2\pi\sigma} \exp\left(-\frac{x^2 + y^2}{2\sigma^2}\right) \quad (15)$$

where σ is the standard deviation of Gaussian kernel. The spread of Gaussian convolution kernel should be larger than $\pm 3\sigma$, according to the statistical three-sigma rule.

The boxcar convolution of the intensity is effectively the low-pass filter with two-dimensional spatial convolution kernel defined as:

Table 3 Droplet gravitational settling velocity and the ratio of terminal velocity to the turbulent velocity fluctuations

d_p (μm)	20	30	40	50	60	70	80	90	100
W (m/s)	0.01	0.03	0.05	0.07	0.10	0.14	0.18	0.23	0.29
$\frac{W}{\sqrt{u_{1,rms}^2 + u_{2,rms}^2}}$									
$Re_\lambda = 107$	0.03	0.07	0.13	0.20	0.29	0.40	0.52	0.66	0.82
$Re_\lambda = 145$	0.03	0.06	0.11	0.17	0.25	0.33	0.44	0.55	0.68
$Re_\lambda = 185$	0.02	0.05	0.08	0.13	0.19	0.26	0.34	0.43	0.54
$Re_\lambda = 213$	0.02	0.04	0.07	0.12	0.17	0.22	0.30	0.38	0.47

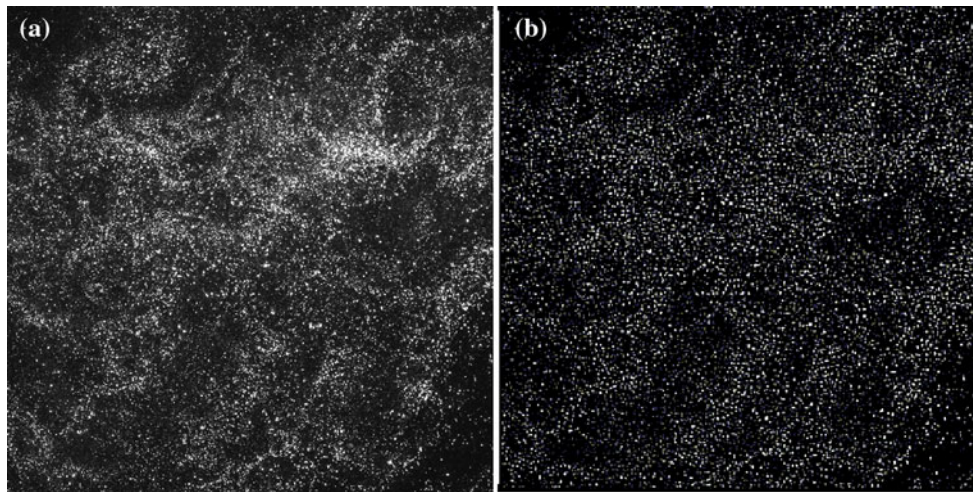


Fig. 4 **a** A typical recorded image of the scattered light intensity from droplets; **b** processed image after band-pass filtering based on Gaussian and boxcar convolution of the intensity

$$F(x,y) = \begin{cases} 1 & -a \leq x \leq +a \quad \text{and} \quad -a \leq y \leq +a \\ 0 & \text{else} \end{cases} \quad (16)$$

where a sets the boundary for boxcar kernel, and x and y represent the local coordinate on the image. The value of a in Eq. (16) corresponds to the spread of Gaussian convolution kernel. The spread of the Gaussian kernel and boxcar kernel should be the same so that effective band-pass filtering can be performed on the image. Details in choosing the spread for the band-pass filter kernels are discussed in the following text.

A typical recorded raw image and the corresponding band-pass filtered image are shown in Fig. 4a, b, respectively. However, the liquid volume loading within the ‘box of turbulence’ cannot be linked with the injected liquid volume from the atomizer, since only a small number of droplets from the original spray enter the ‘box’. Therefore, the droplet number density can only be quantified from the recorded images, and it is not directly linked to the initially injected liquid volume.

The local intensity maxima of the band-pass filtered image were calculated to identify each droplet. This process is presented at Fig. 5a, b.

Successful droplet identification is essential for the quantification of preferential concentration using the RDF or Voronoi analysis. The image processing method applied to each image for droplet identification is summarized in Fig. 6. The process is as follows: (1) import the recorded TIFF formatted image into MATLAB as a UINT8 array and convert the contents of the data set into one array of double precision; (2) the image double precision array is band-pass filtered using a Gaussian convolution as the high-pass and a boxcar convolution as the low-pass

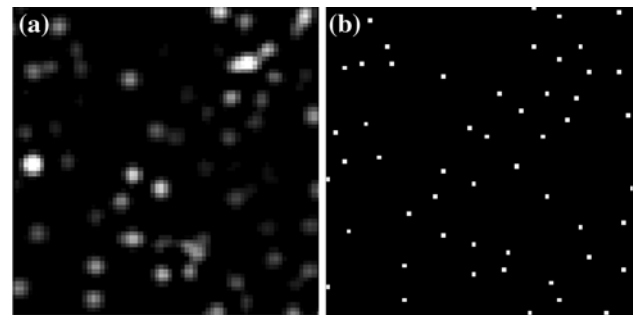


Fig. 5 **a** Band-pass filtered image; **b** locations of local intensity maxima indicating droplets, as required for quantification of droplet clustering

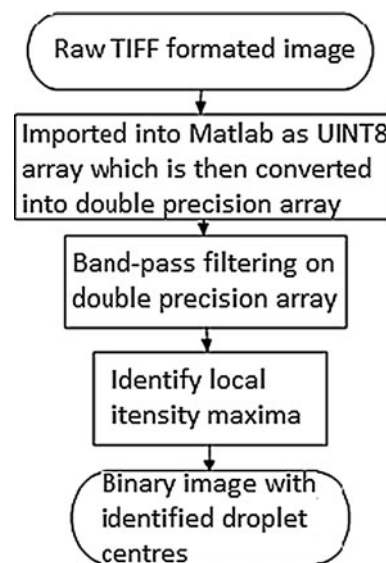


Fig. 6 Image processing procedure for droplet identification

intensity filter; (3) local maxima are calculated from the band-pass filtered image to identify the centre of each droplet; and (4) form the binary image array with the pixel values assigned as 1 for droplet centres and the rest as 0.

In order to determine the optimum image processing parameters for all considered conditions, several instantaneous droplet images were processed with many combinations of image processing parameters. The combination of parameters that resulted in the best visual inspection was further tested through the Q factor criterion and the behaviour of the RDFs, as presented in the text below. The approach used to determine the band-pass filter kernel parameters is discussed below. For the Gaussian kernel, the standard Gaussian distribution with unity standard deviation σ has been applied to the high-pass convolution process, considering that the digitalization noise from the CCD tends to be purely random with a length of one pixel (Crocker and Grier 1996). Then, the spread of the convolution kernel remains the primary parameter in the filtering process. The spread cannot be less than $\pm 3\sigma$, in order to fully represent the values drawn from the Gaussian distribution. For the boxcar kernel, the spread of the effective interval should be the same as that of the Gaussian kernels.

To determine the spread of the effective intervals for the convolution kernel in the band-pass filter process, the non-dimensional universal image quality Q index, proposed by Zhou and Bovik (2002), has been applied to indicate loss of correlation, luminance distortion and contrast distortion between the experimentally acquired images and the band-pass filtered ones. The Q index was defined as follows:

$$Q = \frac{\sigma_{xy}}{\sigma_x \sigma_y} \cdot \frac{2\bar{x} \cdot \bar{y}}{(\bar{x})^2 + (\bar{y})^2} \cdot \frac{2\sigma_x \sigma_y}{\sigma_x^2 + \sigma_y^2} \quad (17)$$

where $x = \{x_i | i = 1, 2, \dots, n\}$ and $y = \{y_i | i = 1, 2, \dots, n\}$ are the digitized intensity signals of the experimentally acquired and the band-pass filtered images, respectively, and

$$\begin{aligned} \bar{x} &= \frac{1}{n} \sum_{i=1}^n x_i; \quad \bar{y} = \frac{1}{n} \sum_{i=1}^n y_i; \\ \sigma_{xy} &= \frac{1}{n-1} \sum_{i=1}^n (x_i - \bar{x})(y_i - \bar{y}); \quad \sigma_x^2 \\ &= \frac{1}{n-1} \sum_{i=1}^n (x_i - \bar{x})^2; \quad \sigma_y^2 = \frac{1}{n-1} \sum_{i=1}^n (y_i - \bar{y})^2 \end{aligned}$$

and n is the one-dimensional image resolution; in our case, n is 1,024.

The first part of the Eq. (17) represents the correlation between two images, the second component represents the luminance distortion, and the last one shows the contrast distortion, since the standard deviation of the intensity can be viewed as estimation of image contrast. When applied to

images, the overall Q index is computed by averaging over each local Q index. Detailed description can be found in Zhou and Bovik (2002).

We evaluate the Q index, shown in Fig. 7, as a function of different spreads of both Gaussian and boxcar convolution kernels. In this way, we can determine the appropriate convolution kernel spread for droplet identification procedure. As shown in Fig. 7, the Q index becomes maximum for a spread ranging from $\pm 5\sigma$ to $\pm 7\sigma$, which indicates that the least loss of correlation, luminance distortion and contrast distortion would be expected for such kernel spread. Based on the Q index evaluation, in order to further determine the unique convolution kernel applied to the band-pass filtering process, we examine the dependence of the detected number of droplets and the droplet clustering value of the RDF [see definition in Eq. (18)] on the spread, for values $\pm 5\sigma$, $\pm 6\sigma$ and $\pm 7\sigma$, of the convolution kernel. The absolute value of Q is affected by luminance distortion and contrast distortion on the acquired images, and this must be corrected in order to identify the droplets correctly. Therefore, the low absolute value quantifies the level of correction that is required. The reduction in the correlation between filtered and original images is due to the correction of distortions, which are larger when the droplet number density increases.

The band-pass filtering process is applied to identify droplets for 8 experiments with turbulent Reynolds number of 185. Each experiment represented by droplet Sauter mean diameter ranging from 25 to 95 microns, including those with wide size distribution spread. Figure 8 shows the average number of detected droplets, quantified from 1,000 images from each experiment. It demonstrates that the number of detected droplets is not greatly affected by the value of convolution kernel spread, especially for large droplet Sauter

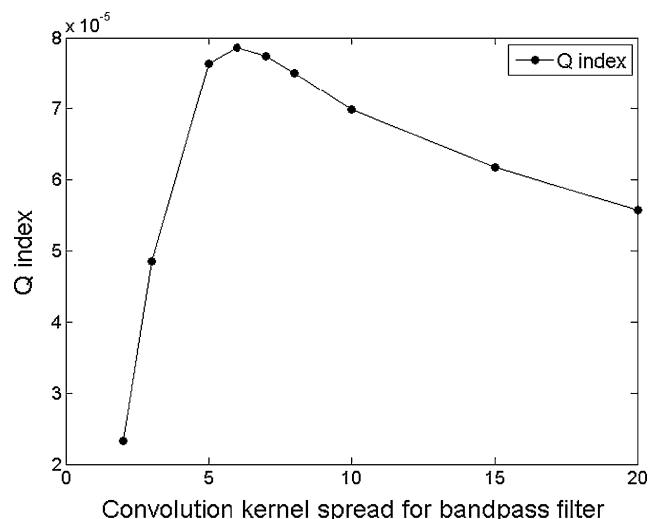


Fig. 7 Non-dimensional universal image quality Q index of Eq. (17) as a function of convolution kernel spread

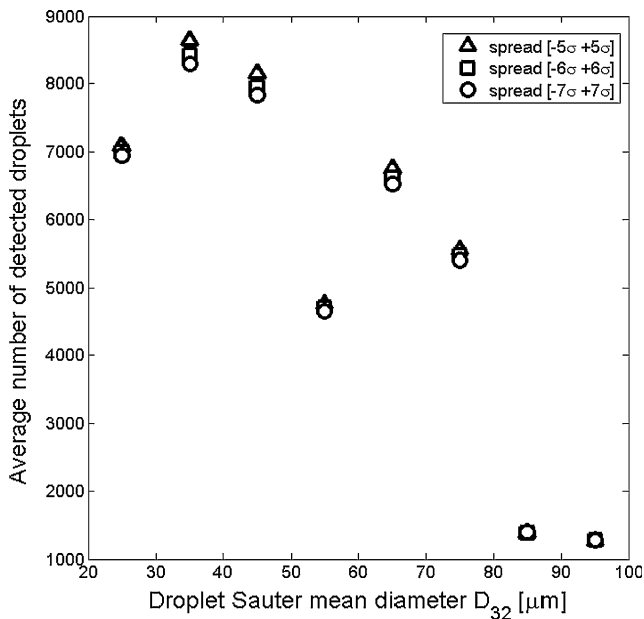


Fig. 8 Number of detected droplets for different kernel spreads for different droplet Sauter mean diameters and turbulent flow of $Re_\lambda = 185$

mean diameters of around 85 and 95 μm . For smaller Sauter mean diameters, $\pm 5\sigma$ kernel spread performs slightly better in detecting droplets, since 2 % more droplets are identified. The average number of droplets for Sauter Mean diameter of 55 microns in Fig. 8 is reduced. This is mainly due to the nonlinear dependence of the atomization process and the operating air and liquid flow rates of the atomizer. Therefore, the combined air and liquid flow rates used to deliver the appropriate Sauter Mean diameter may lead to lower number of droplets being present in the ‘box’. This has also been suggested by Fig. 2f of Monchaux et al. (2010). Therefore, this is not due to measurement uncertainty. The ultimate goal of our image processing is to locate droplets for further quantification of droplet preferential concentration. As a consequence, the sensitivity of the RDF value on the convolution kernel spread is discussed below with the RDF definition provided by Eq. (18) of the next section.

The identified droplet binary images from 8 experiments with different droplet size distributions for turbulent Reynolds number of 185 are further processed to quantify the RDF. Figure 9 shows the calculated averaged RDF from 1,000 images for each experiment, based on band-pass filtering kernel spread of $\pm 5\sigma$, $\pm 6\sigma$ and $\pm 7\sigma$. For each experiment, there are negligible differences in terms of RDF maximum value and the normalized radial distance r/η of the intersecting point with unity RDF value, which represents the cluster length scale. Therefore, once the maximum quality index Q is identified, the convolution kernel spreads have little effect on the RDF. A logarithmic axis has been used in Fig. 9 to improve clarity by reducing

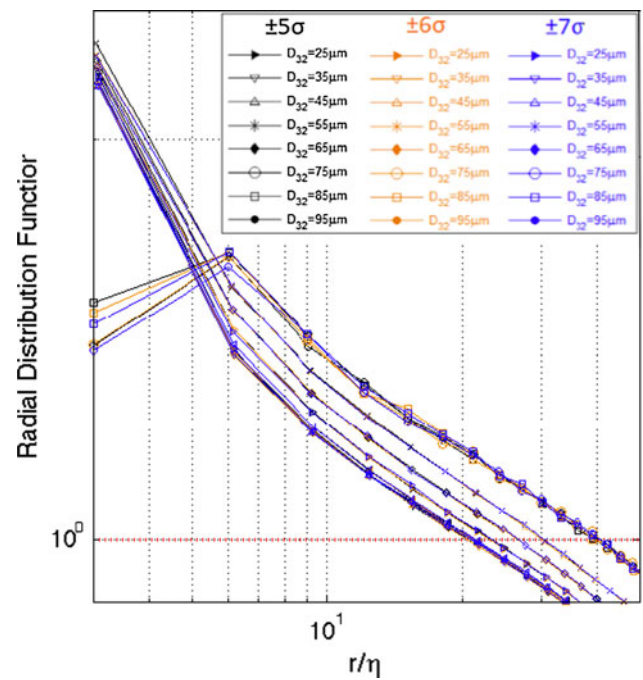


Fig. 9 RDF for different kernel spreads for different Sauter mean diameters for turbulent flow $Re_\lambda = 185$. The radial distance is normalized by the Kolmogorov scale

the overlapping of the symbols and demonstrate that the different image processing parameters do not affect the quantification of droplet clustering.

In summary, possible convolution kernel spreads of the image processing approach for the evaluation of universal image quality Q index are limited to $\pm 5\sigma$, $\pm 6\sigma$ and $\pm 7\sigma$. The evaluation of the influence of the convolution kernels on the average identified droplet number for 8 experiments for the flow with turbulent Reynolds number of 185 showed that $\pm 5\sigma$ spread was slightly more efficient for smaller droplets, while all three spreads performed similarly in identifying larger droplets. Since the final goal is to quantify preferential concentration from the detected droplets on each image, the influence of different convolution kernel spreads on the quantification of the RDF was evaluated. The average RDF from each experiment shows that there is negligible difference when processing images with different band-pass filtering kernel spreads. It should be noted that this result applies to poly-dispersed droplets with a wide range of size spread of the distributions. The following results of preferential concentration quantification are all using droplet identification scheme with a kernel interval spread of $\pm 5\sigma$.

We have not performed a detailed study of the effects of droplet number density and optical noise on the image processing method. This must be performed by reference particle images, similar to the approach used by Okamoto et al. (2000) for PIV error evaluation. This was beyond the focus of the current paper.

3 Stokes number scaling of droplet clustering

3.1 Radial distribution function (RDF) and Voronoi analysis

The preferential droplet concentration was quantified by using two methods, namely the RDF and two-dimensional Voronoi analysis.

The RDF was proposed by Sundram and Collins (1999) and defined as:

$$\text{RDF} = \frac{N(r_i)A}{A(r_i)N} \quad (18)$$

where $N(r_i)$ is the number of droplets in a ring with width of $2dr$ and radius r_i from the centre of a randomly selected droplet. $A(r_i)$ is the area or volume of the ring between $r - dr$ and $r + dr$, A is the total area or volume of the considered image, and N is the total number of droplets. The RDF indicates the droplet number density within a ring of certain radius relative to the average droplet number density in the area of interest. Increased droplet relative concentration in a ring of a given radius leads to increased RDF value. The relative number density is unity for randomly distributed droplets and always above unity for preferentially concentrated droplets. The minimum distance around $r/\eta = 0$ of the RDF is around 3–4, which is determined by the spatial resolution and the number density of the droplets in the flow. The selection of dr is a compromise between having enough droplets within each of the ‘rings’ of the RDF and maintaining appropriate spatial resolution. Provided that the RDF converges after averaging over all images, the resulting function will be independent of dr . Examples of RDFs for a range of experiments with turbulent Reynolds number of 185 are shown in Fig. 10. The RDF values for droplet Sauter mean diameter D_{32} of 55 μm at each radius are larger than those for other experimental conditions. Thus, according to the definition of the RDF, the strongest preferential concentration in this flow occurs for droplet size distribution with Sauter mean diameter D_{32} of 55 μm . The RDF for D_{32} of 65 μm has the second largest value, as shown in Fig. 10, while the other conditions appear to have similar degree of preferential concentration with overlapping RDF curves.

The radial distance where the RDF value becomes unity can be viewed as a statistical description of the characteristic length scale of the droplet clusters. Therefore, Fig. 10 shows that, for flow with $Re_\lambda = 185$, the droplet cluster length scale varies between 20 and 30 η , where η is the Kolmogorov length scale. The largest cluster length scale of 30 η occurs for droplets with D_{32} of 55 μm , which also have the highest magnitude of preferential concentration. This suggests a positive relation may exist between the degree of clustering and the characteristic cluster length scale. Similar

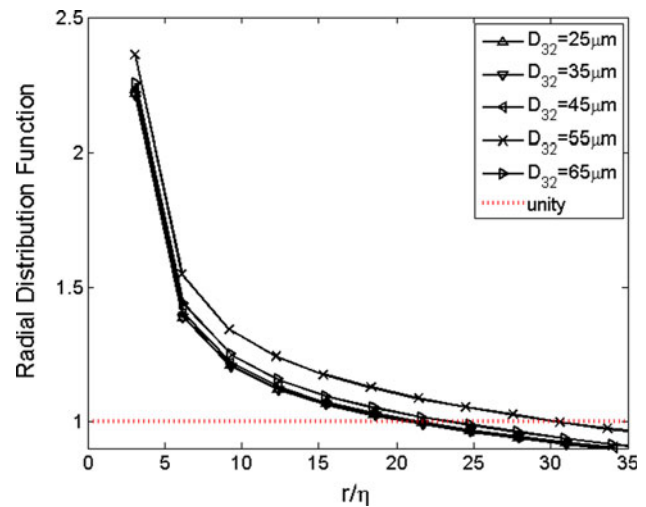


Fig. 10 RDFs for different droplet size distributions and flow with turbulent Reynolds number of 185

range of cluster length scale was observed for flows with $Re_\lambda = 107$, 145 and 213, also with a positive correlation between degree of clustering and characteristic cluster length scale. It should be noted that the characteristic cluster length scales measured for mono-sized particles are of the order of 10η (Fessler et al. 1994; Aliseda et al. 2002; Wood et al. 2005; Saw et al. 2008; Monchaux et al. 2011), which is of similar order of magnitude as the present results. A positive relation may exist between the degree of clustering and the characteristic cluster length scale. However, techniques in defining cluster size and further experiments need to be developed and performed to reveal the relationship between cluster size and other quantities.

The Voronoi analysis decomposes two-dimensional space into individual Voronoi cells that correspond to each detected droplet with ensemble points closer to it than any other droplets. Figure 11a is a typical image with identified droplets. Due to the large number of droplets per image, we present part of the recorded image for better illustration. Figure 11b shows the droplet centres with associated Voronoi cells. The Voronoi cell area A is the inverse of the local droplet concentration. Thus, the distribution function of Voronoi cell area can provide information of local droplet concentration. The distribution function of the normalized Voronoi cell areas A/A_{avg} has been applied to the quantification of preferential concentration (Monchaux et al. 2010).

The distribution function of normalized Voronoi cell areas of randomly distributed droplets is represented by random poisson process (RPP), defined by Eq. (19) (Ferenc and Neda 2007), where y is the normalized Voronoi cell areas.

$$f2D(y) = \frac{343}{15} \sqrt{\frac{7}{2\pi}} y^{\frac{5}{2}} \cdot e^{\left(-\frac{7}{2y}\right)} \quad (19)$$

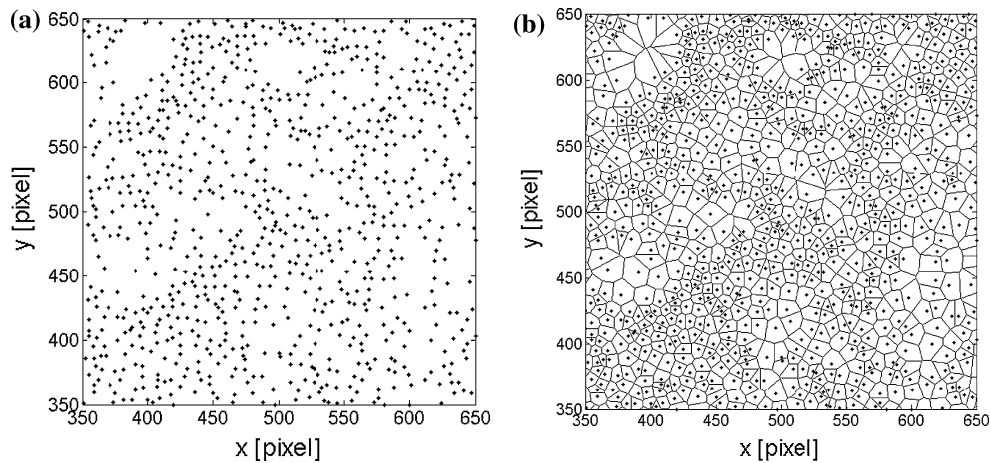


Fig. 11 **a** Typical (part of) image with identified droplet centres; **b** droplet centres with associated Voronoï areas

The standard deviation of RPP of Voronoï areas is known to be $\sigma_{RPP} = 0.53$. For preferentially concentrated droplets, the standard deviation of Voronoï areas is larger than σ_{RPP} . Larger increase in the standard deviation above the value of 0.53 indicates stronger preferential concentration.

The normalized probability density functions (PDFs) of Voronoï areas, for different size distributions and for flow with turbulent Reynolds number of 185, are shown in Fig. 12a. The dashed line represents the RPP distribution function in Fig. 12a. The results show that the measured PDFs clearly depart from RPP, which indicates the presence of droplet preferential concentration. The standard deviation of the normalized Voronoï areas, averaged over 1,000 images for each experimental condition, was calculated for different droplet Sauter mean diameters and is presented in Fig. 12b for flow with turbulent Reynolds number of 185 as a function of droplet Sauter mean diameter. All the standard deviations are larger than 0.53, the corresponding RPP value, confirming the presence of preferential concentration. The results also show that the maximum value of standard deviations and, therefore, the strongest preferential concentration occurs for droplet size distribution with D_{32} of 55 μm . The second largest is for D_{32} of 65 μm , while the other conditions appear to have similar degree of preferential concentration since the standard deviation of the normalized Voronoï area does not vary, in agreement with observations from the RDF analysis (Fig. 10).

3.2 Droplet Stokes number scaling

The Stokes number, defined in Eq. (20), is the primary parameter used to scale preferential concentration.

$$St = \frac{\tau_p}{\tau_k} = \left(\frac{d}{\eta} \right)^2 \frac{(1 + 2\Gamma)}{36} \quad (20)$$

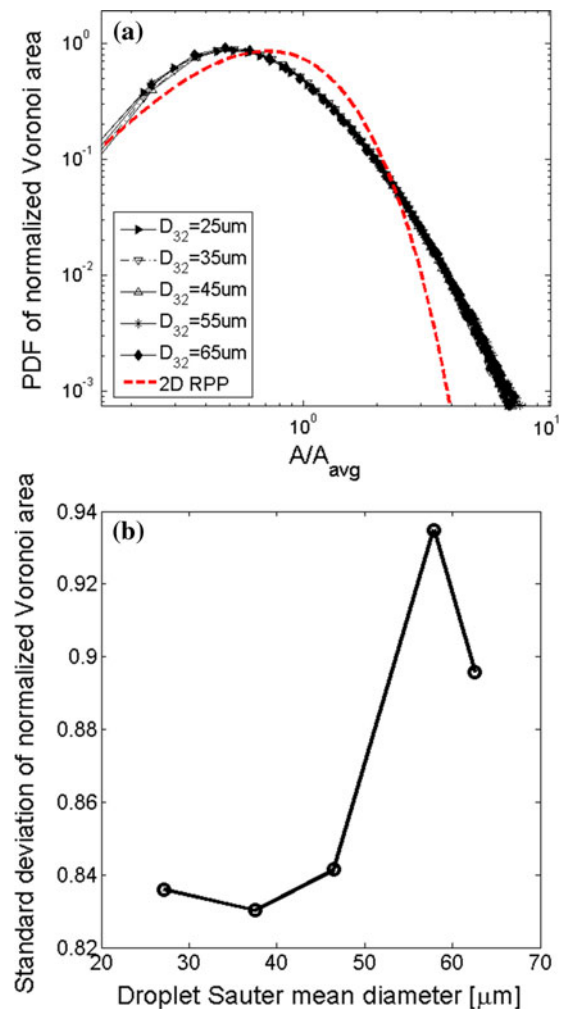


Fig. 12 **a** Normalized PDFs of Voronoï areas for different droplet size distributions. The PDF for RPP is superimposed as *dashed line*; **b** standard deviation of normalized Voronoï area as a function of droplet Sauter mean diameter. The standard deviation for RPP is 0.53. Flow with turbulent Reynolds number of 185

where τ_p represents the droplet response time, τ_k is a characteristic turbulent timescale, and d and η are the droplet diameter and characteristic turbulent length scale, respectively. The characteristic flow timescale was selected to be the Kolmogorov timescale as many previous workers (Wang and Maxey 1993; Fallon and Rogers 2002; Wood et al. 2005). Γ denotes the density ratio between the dispersed and the carrier phase.

For poly-dispersed droplet-laden flows, the presence of various droplet size distributions with different mean diameters and size spreads results in large variation of the value of the Stokes number. In order to identify a representative droplet Stokes number for each size distribution and link it to resulting preferential droplet concentration, it is desirable to establish an appropriate diameter of the measured droplet size distribution for which the Stokes number will describe appropriately the clustering behaviour of the polydispersed droplets.

For mono-sized particle-laden flows, it has been found both numerically and experimentally that the strongest preferential concentration occurs when the Stokes number is around unity (Crowe et al. 1985; Maxey 1987; Hardalupas et al. 1990, 1992; Squires and Eaton 1991; Longmire and Eaton 1992; Eaton and Fessler 1994; Wood et al. 2005; Salazar et al. 2008; Saw et al. 2008; Monchaux et al. 2010; Bateson and Aliseda 2012). Studies with poly-dispersed droplets tend to conclude ambiguously that the strongest preferential concentration occurs when the Stokes number is significantly different than unity. For example, Monchaux et al. (2010) considered poly-dispersed droplet-laden flows and reported that the strongest preferential concentration occurs for St around 2–3. The fact that the Stokes number deviates from unity, when strongest preferential concentration occurs, is due to the selection of the representative diameter of the size distribution that was used for the calculation of the droplet Stokes number of Eq. (20). Therefore, for poly-dispersed droplets, an evaluation of the resulting Stokes number values, based on different droplet representative diameters of the size distribution, is required. Thus, we compare the values of the Stokes number based on droplet mean diameters D_{10} , D_{32} defined in Eq. (12), number-weighted droplet diameter $DN_{40\%}$ and $DN_{60\%}$, and volume-weighted droplet diameter $DV_{5\%}$ and $DV_{50\%}$, which have all been defined in Sect. 2. The relative relation of those characteristic droplet diameters is shown in Fig. 13, based on the definition from Sect. 2.

The standard deviation of the variation of the normalized Voronoï areas as a function of droplet Stokes number for flow with $Re_\lambda = 185$ is presented in Fig. 14c. Each line corresponds to the estimation based on a different characteristic droplet diameter. Figure 14c shows that the standard deviation of the Voronoï areas, which indicates the degree of preferential concentration, becomes maximum

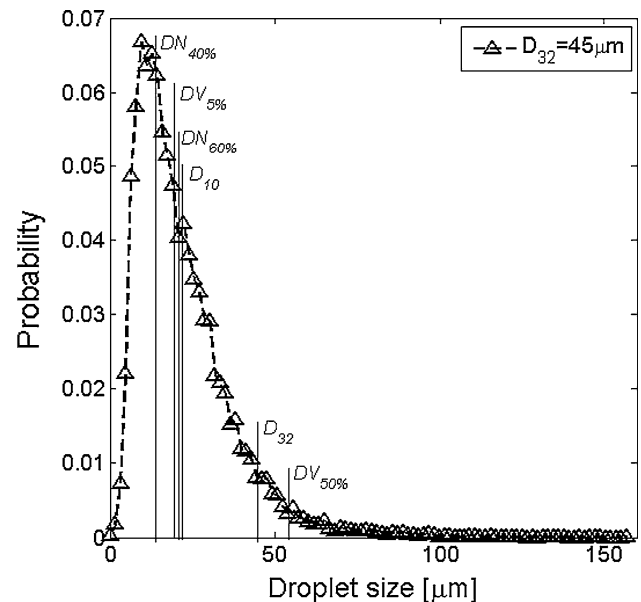
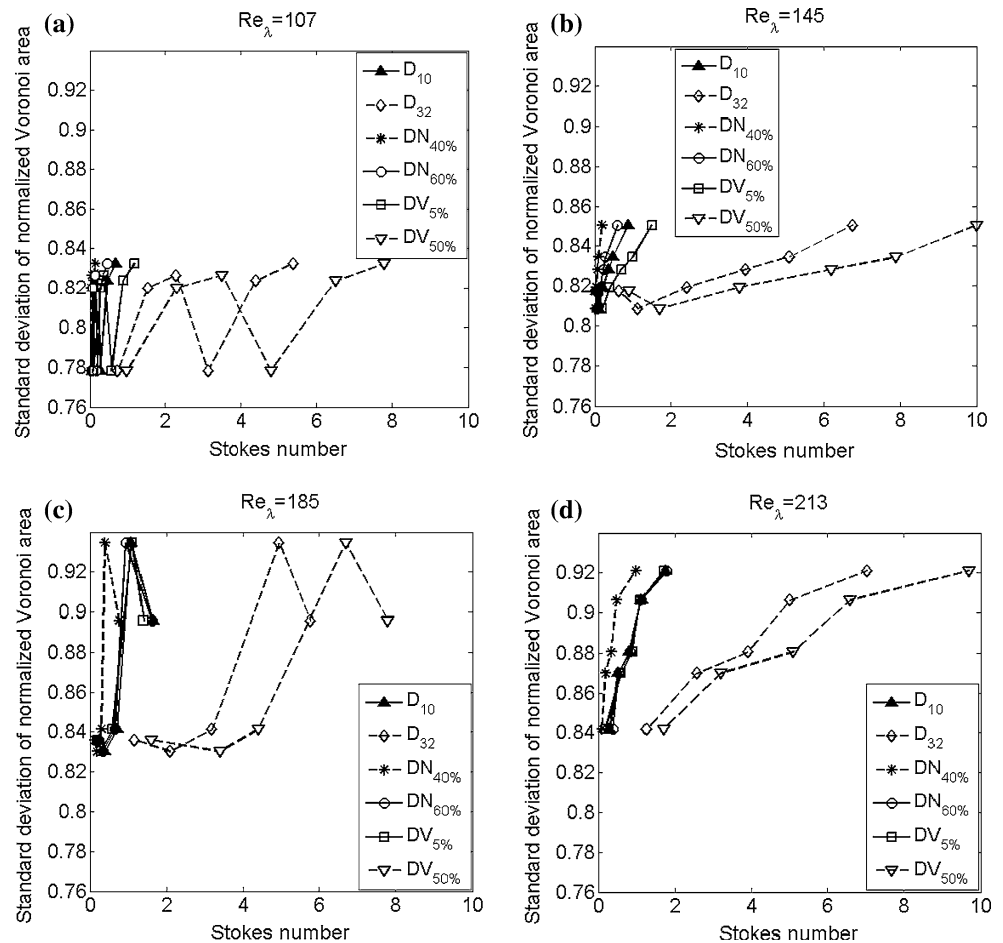


Fig. 13 Number-weighted droplet size distribution for the case with Sauter mean diameter of 45 μm with vertical lines indicating the various characteristic droplet diameters

for corresponding droplet Stokes numbers ranging from 0.5 to 10 for experiments with $Re_\lambda = 185$. This wide range of values demonstrates why previous studies have observed variability at the value of the Stokes number for which the strongest preferential concentration occurs. This also demonstrates the need to identify the representative diameter for a poly-dispersed droplet size distribution that is appropriate for the definition of the Stokes number, so that it can be around unity when maximum preferential concentration is observed. It should be noted that the standard deviation of the normalized Voronoï area is an unambiguous parameter indicating the degree of droplet clustering. With the large amount of experimental data presented, it is desirable to base the analysis on such a quantity rather than the trends of the RDF curve. Therefore, the current section focuses only on the Voronoï analysis. Quantifications based on RDF are included in order to provide comparisons with the results from the Voronoï data and estimation of the cluster length scale. The agreement between the two approaches supports better our findings.

Figure 14c shows that three droplet representative diameters, namely D_{10} (arithmetic mean), $DN_{60\%}$ (the diameter below which 60 % of the total number of droplets in the spray is present) and $DV_{5\%}$ (the diameter which carries 5 % of the liquid volume in the spray), lead to the least bias from the unity value of Stokes number when the standard deviation of Voronoï areas is maximized. The results for the three different turbulent conditions with $Re_\lambda = 107$, 145 and 213 are shown in Fig. 14a, b, d respectively. We can also observe ascending curves of standard deviation of Voronoï areas with Stokes number,

Fig. 14 Standard deviation of the Voronoï area as a function of droplet Stokes number, defined according to various representative diameters of the droplet size distribution, for flows with turbulent Reynolds numbers of 107, 145, 185 and 213



except of one stand-alone point for $Re_\lambda = 107$, which is more likely due to experimental uncertainty. Figure 14a, b, d also show that the rising curves of standard deviations become maximum for a droplet Stokes number around unity, when the Stokes number is based on D_{10} , $DN_{60\%}$ and $DV_5\%$. Attempts to scale droplet preferential concentration with a Stokes number based on other droplet diameters lead to ascending curves of standard deviation of Voronoï areas for droplet Stokes numbers much larger than unity, which is not expected from theoretical and experimental studies with mono-sized particles. It should be noted that Fig. 14 shows that the droplet distribution always has a non-random component and the standard deviation of the Voronoï areas never approaches 0.53 (the value for random distributions) for small Stokes numbers. This is because the droplet Stokes number never becomes small enough to eliminate the preferential concentration. However, when the same analysis was applied to the concentration of ‘seeding’ particles, introduced in the flow for PIV measurements of the flow turbulence characteristics, their distribution was always random.

It may be suggested that the consideration of around 60 % of the total number of droplets in a poly-dispersed

spray is appropriate to scale the preferential concentration. However, when considering a volume-based description of the size distribution, the diameter carrying 5 % of the total liquid volume is appropriate for the identification of the preferential droplet concentration. This suggests that preferential concentration occurs mainly for droplet sizes that carry around 5 % of the liquid volume of the spray, which raises some questions about the practical significance of preferential concentration.

The most probable droplet diameter has been used in the poly-dispersed clustering study of Monchaux et al. (2010). The most probable droplet diameter does not necessarily have a response timescale similar to the Kolmogorov timescale for which the strongest preferential concentration appears. The Stokes numbers based on D_{10} , $DN_{60\%}$ and $DV_5\%$ are similar, and it appears that the strongest preferential concentration occurs when the Stokes number derived from the representative droplet diameters is around unity. Thus, we propose the use of D_{10} , $DN_{60\%}$ and $DV_5\%$ in studying clustering of the poly-dispersed droplets with certain size spread shape. It is possible that the dynamics of the droplets with such diameters governs the overall clustering behaviour of the poly-dispersed phase.

Despite the wide range of conditions of the current study, further evaluation is required for the verification of the generality of the proposed representative diameters for scaling of preferential concentration at different flows and sprays and the associated practical significance.

It should be noted that the size of most droplets studied is less than 150 microns (refer to Fig. 3a), while the Kolmogorov length scale for all flow conditions is larger than 180 microns (refer to Table 1). We also consider very dilute suspension with the volume fraction (Elghobashi 1994) in the range of 10^{-6} . Thus, the finite size effect (Qureshi et al. 2007) and the collective effect (Aliseda et al. 2002) do not affect the droplet clustering behaviour in the presented work.

The current conclusions are related to the observed shape of the droplet size distribution, which is typical for a wide range of sprays. However, if the shape of the size distribution deviates completely from the observed shapes in the current work, the appropriate representative diameters may change.

4 Effect of turbulent Reynolds number on droplet clustering

The previous section proposed a droplet Stokes number based on D_{10} , $DN_{60\%}$ and $DV_5\%$ to scale preferential concentration. In the current section, we will use this droplet Stokes number to evaluate the influence of the turbulent Reynolds number on preferential concentration.

The standard deviation of the Voronoï areas, representing the degree of droplet clustering, as a function of the Stokes number, based on $DN_{60\%}$, for different turbulent Reynolds number is presented in Fig. 15. Error bars indicate the corresponding statistical uncertainties for a confidence level of 95 %. It is obvious that the statistical errors are relatively large, so that it appears to be little dependence of preferential concentration on flow turbulent intensities. Droplets appear to cluster more, as the Stokes number is approaching unity for different flow turbulent intensity. Although some scatter is present in the results, the degree of preferential concentration appears to have little dependence on flow turbulent intensities. This finding is in contrast to a recent DNS simulation by Tagawa et al. (2012), which proposed that both light and heavy particles tend to have stronger preferential concentration for more intense flow turbulence. A recent experimental work by Obligado et al. (2011) covered a wider range of Stokes number and suggested that there might be a positive dependence of preferential concentration on the turbulent Reynolds number. However, in our case, due to the presence of uncertainties and lack of data points at higher Stokes number range, we could not see such a trend. Based

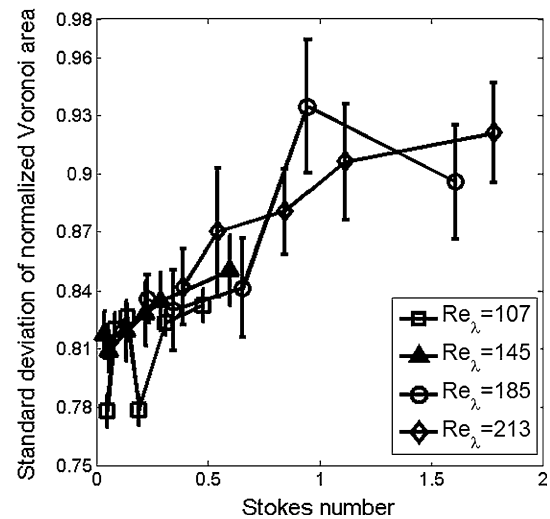


Fig. 15 Variation of standard deviation of Voronoï areas as a function of droplet Stokes number, based on $DN_{60\%}$, for flows with turbulent Reynolds number of 107, 145, 185 and 213. Error bars indicate the statistical uncertainties for a confidence level of 95 %

on the presented data, there seems to be little dependence of the standard deviation of Voronoï areas on the turbulent Stokes number. Thus, more experiments covering a wider range of droplet Stokes numbers and turbulent Reynolds numbers is required to evaluate the effect of turbulent intensity on preferential concentration.

5 Summary

The preferential concentration of poly-dispersed droplets with Sauter mean diameter between 25 and 95 μm with four different flow turbulent intensities ($Re_\lambda = 107, 145, 185$ and 213) has been studied. A band-pass filter-based image processing method is proposed for the identification of droplet locations on images of scattered light intensity from droplets. The effectiveness of the method was assessed for various image qualities, and the influence of the image processing parameters was evaluated on the quantification of droplet clustering. RDF and Voronoï analysis were applied to quantify droplet preferential concentration. An appropriate Stokes number for poly-dispersed droplets is proposed for scaling of droplet clustering and the role of turbulence on clustering behaviour is discussed. A summary of the findings is listed below.

1. The influence of image processing parameters of a band-pass filter method to detect droplet locations and quantify droplet clustering was presented and verified by considering the universal image quality Q index. This allowed the quantification of the degree of droplet preferential

concentration for poly-dispersed droplets with wide range of size distributions, as summarized in Table 2.

2. The preferential concentration was quantified by the RDF method and Voronoï analysis and the results are in agreement. It was concluded that the strongest preferential concentration occurred when a proposed Stokes number, based on D_{10} (the arithmetic mean droplet diameter), $DN_{60} \%$ (the diameter associated with 60 % of the total number of droplets in the spray) or $DV_5 \%$ (the diameter that carries 5 % of the liquid volume in the spray), is around unity. This suggests that the preferential concentration of poly-dispersed droplets is governed by the sizes carrying a large number of fraction of droplets and a small fraction of liquid volume in a spray. The latter raises some questions on the practical significance of preferential concentration.
3. The RDF method indicated that the length scale of droplet clusters varies between 20 and 30 times the Kolmogorov length scale of the flow turbulence for all size distributions and flow conditions. This is of the same order of 10 times the Kolmogorov scale for mono-sized particles of previous studies (Fessler et al. 1994; Aliseda et al. 2002; Wood et al. 2005).
4. Droplet preferential concentration appears to have little dependence on turbulent Reynolds number when the proposed Stokes number remains the same. This finding is in contrast to recent DNS results (Tagawa et al. 2012), which suggests that further investigation of the effect of turbulence is required.

Acknowledgments Financial support from Engineering and Physical Sciences Research Council (EPSRC) under Grant EP/E029515/1 is acknowledged. HL has received financial support from the China Scholarship Council (CSC). Finally, support is acknowledged from the European Union COST Action MP0806.

References

- Aliseda A, Cartellier A, Hainaux F, Lasheras JC (2002) Effect of preferential concentration on the settling velocity of heavy particles in homogeneous isotropic turbulence. *J Fluid Mech* 468:77–105
- Balachandar S, Eaton JK (2010) Turbulent dispersed multiphase flow. *Annu Rev Fluid Mech* 42:111–133
- Batchelor GK (1953) The theory of homogeneous turbulence. Cambridge University Press, Cambridge
- Bateson CP, Aliseda A (2012) Wind tunnel measurements of the preferential concentration of inertial droplets in homogeneous isotropic turbulence. *Exp Fluids* 52:1373–1387
- Bayvel L, Orzechowski Z (1993) Liquid atomization, 1st edn. Taylor and Francis Ltd, London
- Birouk M, Chauveau C, Sarh B, Quilgars A, Gokalp I (1996) Turbulence effects on the vaporization of monocomponent single droplets. *Combust Sci Tech* 113–114:413–428
- Bordás R, Hagemeyer T, Wunderlich B, Thévenin D (2011) Droplet collisions and interaction with the turbulent flow within a two-phase wind tunnel. *Phys Fluids* 23:085105
- Charalampous G, Hardalupas Y (2010) Clustering of mono-disperse and poly-disperse particles in a “box of turbulence”. 7th ICMF 2010, Tampa, FL USA
- Crocker JC, Grier DG (1996) Methods of digital video microscopy for colloidal studies. *J Colloid Interface Sci* 179:298
- Crowe CT, Gore RA, Troutt TR (1985) Particle dispersion by coherent structures in free shear flows. Part Sci Technol 3:149–155
- Eaton JK, Fessler JR (1994) Preferential concentration of particles by turbulence. *Int J Multiph Flow* 20:169–209
- Elghobashi S (1994) On predicting particle-laden turbulent flows. *Appl Sci Res* 52:309–329
- Fallon T, Rogers CB (2002) Turbulence-induced preferential concentration of solid particles in microgravity conditions. *Exp Fluids* 33:233–241
- Ferenc JS, Neda Z (2007) On the size distribution of poisson Voronoï cells. *Phys A* 385:518–526
- Fessler JR, Kulick JD, Eaton JK (1994) Preferential concentration of heavy particles in a turbulent channel flow. *Phys Fluids* 6:3742–3749
- George WK (2006) Lectures in turbulence for the 21st century. Chalmers University of Technology, Gothenburg
- Goepfert C, Marié JL, Chareyron D, Lance M (2009) Characterization of a system generating a homogeneous isotropic turbulence field by free synthetic jets. *Exp Fluids* 48:809–822
- Hardalupas Y, Taylor AMKP, Whitelaw JH (1990) Velocity and size characteristics of swirling liquid-fuelled flames. *Proc R Soc Lond A* 428:129–155
- Hardalupas Y, Taylor AMKP, Whitelaw JH (1992) Particle dispersion in a vertical round sudden expansion flow. *Phil. Trans R Soc Lond A* 341:411–442
- Hwang W, Eaton JK (2004) Creating homogeneous and isotropic turbulence without a mean flow. *Exp Fluids* 36:444–454
- Jong J, Cao L, Woodward S, Salazar J, Collins L, Meng H (2008) Dissipation rate estimation from PIV in zero-mean isotropic turbulence. *Exp Fluids* 46:499–515
- Lefebvre AH (1989) Atomisation and sprays. Taylor and Francis Ltd, London
- Longmire EK, Eaton JK (1992) Structure of a particle-laden round jet. *J Fluid Mech* 236:217–257
- Maxey MR (1987) The gravitational settling of aerosol particles in homogeneous turbulence and random flow field. *J Fluid Mech* 174:441–465
- Monchaux R, Bourgoïn M, Cartellier A (2010) Preferential concentration of heavy particles: a Voronoï analysis. *Phys Fluids* 22:103304
- Monchaux R, Bourgoïn M, Cartellier A (2011) Analyzing preferential concentration and clustering of inertial particles in turbulence. *Int J Multiph Flow* 40:1–18
- Obligado M, Missaoui M, Monchaux R, Cartellier A, Bourgoïn M (2011) Reynolds number influence on preferential concentration of heavy particles in turbulent flow. *J Phys Conf Ser*, ETC13, Warsaw, Poland: Sept 12–15, 2011 10.1088/1742-6596/318/5/052015
- Okamoto K, Nishio S, Saga T, Kobayashi T (2000) Standard images for particle image velocimetry. *Meas Sci Technol* 11:685–691
- Qureshi NM, Bourgoïn M, Baudet C, Cartellier A, Gagne Y (2007) Turbulent transport of material particles: an experimental study of finite size effects. *Phys Rev Lett* 99(18):184502
- Salazar JPLC, Collins LR (2009) Two-particle dispersion in isotropic turbulent flows. *Annu Rev Fluid Mech* 41:405–432
- Salazar JPLC, Jong JD, Cao LJ, Woodward SH, Meng H, Collins LR (2008) Experimental and numerical investigation of inertial particle clustering in isotropic turbulence. *J Fluid Mech* 600:245–256
- Saw EW, Shaw RA, Ayyalasomayajula S, Chuang PY, Gylfason A (2008) Inertial clustering of particles in high-Reynolds-number turbulence. *Phys Rev Lett* 100:214501

- Shaw RA, Reade WC, Collins LR, Verlinde J (1998) Preferential concentration of cloud droplets by turbulence: effects on the early evolution of cumulus cloud droplet spectra. *J Atmos Sci* 55:1965–1976
- Siebert H, Gerashchenko S, Gylfason A, Lehmann K, Collins LR, Shaw RA, Warhaft Z (2010) Towards understanding the role of turbulence on droplets in clouds: in situ and laboratory measurements. *Atmos Res* 97:426–437
- Squires KD, Eaton JK (1991) Preferential concentration of particles by turbulence. *Phys Fluids* 3:1169
- Sundram S, Collins LR (1997) Collision statistics in an isotropic particle-laden turbulent suspension. Part 1. Direct numerical simulations. *J Fluid Mech* 335:75–109
- Sundram S, Collins LR (1999) A numerical study of the modulation of isotropic turbulence by suspended particles. *J Fluid Mech* 379:105–143
- Tagawa Y, Mercado MJ, Prakash NV, Calzavarini E, Sun C, Lohse D (2012) Three-dimensional Lagrangian Voronoï analysis for clustering of particles and bubbles in turbulence. *J Fluid Mech* 693:201–215
- Tate RW (1982) Some problems associated with the accurate representation of drop-size distributions. In: *Proceedings of 2nd international conference on liquid atomization and spraying systems (ICLSS, Madison)*, 341–351
- Teutolsky SA, Vetterling WT, Flannery BP (1992) *Numerical recipes*. Cambridge University Press, Cambridge
- Wang LP, Maxey MR (1993) Settling velocity and concentration distribution of heavy particles in homogeneous isotropic turbulence. *J Fluid Mech* 256:27–68
- Wood A, Hwang W, Eaton JK (2005) Preferential concentration of particles in homogeneous and isotropic turbulence. *Int J Multiph Flow* 31:1220–1230
- Zhou W, Bovik AC (2002) A Universal Image Quality Index. *Signal Processing Letters, IEEE* 9(3):81–84
- Zimmer L, Domann R, Hardalupas Y, Ikeda Y (2003) Simultaneous laser induced fluorescence and Mie scattering for droplet cluster measurements. *AIAA J* 41:2170–2178